



# Microstructure and characterization of Ti–Al explosive welding composite plate

Zhi-Xiong Bi<sup>1,2</sup> · Xue-Jiao Li<sup>2</sup> · Ting-Zhao Zhang<sup>2</sup> · Quan Wang<sup>2</sup> · Kai Rong<sup>2</sup> · Xian-De Dai<sup>2</sup> · Yong Wu<sup>2</sup>

Received: 17 December 2021 / Accepted: 21 August 2022 / Published online: 21 October 2022  
© The Author(s), under exclusive licence to Springer-Verlag London Ltd., part of Springer Nature 2022

## Abstract

The interface characteristics and microstructure formation of TA2-5083 composite plate after explosive welded were studied. Optical microscope and electron microscope were used to analyze the microstructure of intermetallic compounds. Furthermore, ANSYS/AUTODYN was adopted to calculate the characteristics of interface microstructure simulated by the smooth-particle hydrodynamics (SPH) method. The results show that most molten metal in the wave front stays in the wave-waist region. There was a relative velocity difference between the vortex of molten metal and the titanium tissue, resulting in that broken titanium particles being scoured by vortexes.  $Ti_3Al$  was generated in the vortex, whose antioxidant capacity would lead to the formation of cracks. Consider soldering in a vacuum environment or adding an intermediate layer to reduce interfacial defects. The temperature of the outer vortex was higher than that of inner vortex, and the vortex has a transition layer of 5  $\mu m$ , which is thinner than the transition layer of 10  $\mu m$  between the fly and base plate. The jet of molten metal was mostly composed of aluminum, with the jet velocity of interface reaching 3000  $m \cdot s^{-1}$  and the interface temperature rising up to 2100 K. Compared with the molten metal in the wave-back vortex, the jet temperature at the interface was higher, resulting in a thicker transition layer at the bonding surface.

**Keywords** Explosive welding · Ti–Al composite plate · Numerical simulation · Microstructure · Interfacial characterization

## 1 Introduction

Explosive welding is an excellent bonding technique for dissimilar metals [4], which can improve the corrosion resistance [5], fatigue resistance [1, 9], and mechanical properties [2] of a single material. The element diffusion and microstructure of the joint have great influence on the overall properties of the composite plate [3]. High temperature and high pressure are formed on the surface of the two metals when the cladding plate collides with the substrate at high velocity after explosion. In this environment, there may be grain deformation, crack, vortex and molten block, etc. at the interface of the bimetallic [6–8]. Previous studies have found that collision produces molten metal flow, leading to

mixing and element diffusion, which is an important cause of molten blocks formation [5, 10]. The high-temperature melting and diffusion result in metallurgical bonding of the composite plate [12]. Element diffusion balances the properties of composite plates and improves joint properties [11]. The super-cooling rate of the temperature plays an important role in the formation of the grains in the molten block [3], which causes the grains at the interface to deform, bend, and deflect under the stress wave [5]. Due to the interface characteristics, dislocation slip, crystal twin and shear band, etc. occur, which will cause greater strain on the grain and lead to the reduction of grain size [10].

In the study of Ti–Al composite plate interface, Chulist et al. [13] found that there was a strong asymmetry between the fly and base plate in the welding process, which led to more fine grains in the fly plate compression than in the base plate. The molten metal cools and recrystallizes to form grains, and the formation of intermetallic compounds leads to the fining of grains [12]. Cui et al. [15] found that aluminum matrix composites also had fine grain structure, and the grain refinement is more obvious near the titanium side. Zhang et al. [12] found that the formation of free energy in

✉ Xue-Jiao Li  
xjli@aust.edu.cn

<sup>1</sup> School of Civil Engineering, Anhui University of Science & Technology, Huainan 232001, People's Republic of China

<sup>2</sup> School of Chemical Engineering, Anhui University of Science & Technology, Huainan 232001, People's Republic of China

**Table 1** Chemical composition of TA2 titanium plate

Elements	Fe	C	N	H	O	It
Content/%	≤0.3	≤0.1	≤0.05	≤0.015	≤0.03	Bal.

the bonding zone was low, which led to the formation of intermetallic compounds such as  $Al_3Ti$ .  $Al_3Ti$  and Ti matrix form a semi-coherent interface, which can improve the bonding strength of composite plate [12]. However,  $Ti_3Al$  with higher formability can also be formed at local high temperature. Qin et al. [14] found that cracks occur more frequently in intermetallic compounds and stop propagating at the bonding interface. The intensive swirling of the molten metal results in initial defects such as voids and microcracks [12]. Cui et al. [15] believed that the Ti matrix inhibited the crack propagation. Kwasniak and Garbacz [17] found that almost all alloying elements improved the ductility of  $Ti_3Al$ , but Mg and Sn increased the brittleness of Ti–Al intermetallic compounds. However, few studies were conducted on the effect of interface characteristics on the microstructure formation of Ti–Al composite plates.

In this paper, explosive welding was carried out with TA2 titanium being the fly and 5083 aluminum plate being the base plate. Optical microscope (OM), scanning electron microscope (SEM), and energy-dispersive spectroscopy (EDS) were used to study the initial defects and interface microstructure morphology of the composite plate, and ANSYS/AUTODYN was used to simulate the interface characteristics of the composite plate. The conditions for the formation of intermetallic compounds and initial defects were studied based on interface parameters.

## 2 Materials and models

### 2.1 Explosive welding

Hollow glass microspheres were used as diluents to prepare emulsified explosive with a detonation velocity of  $2475 \text{ m}\cdot\text{s}^{-1}$  as welding charge. A TA2 titanium plate with 1.5 mm thickness was used as the composite plate, and its chemical composition was shown in Table 1. A 5083 aluminum plate with 8 mm thickness was used as the base plate; its chemical composition was shown in Table 2. The charging density was  $522 \text{ kg}\cdot\text{m}^{-3}$ , the thickness of emulsified explosive was 16 mm, and the welding area was  $150 \text{ mm}\times 200 \text{ mm}$ . The horizontally mounted construction was adopted, and the distance between the titanium plate

and aluminum plate was 2 mm. The welding surface of the fly and base plate was polished and cleaned with emery paper and alcohol, and the contact surface of the fly plate and explosive was smeared with butter. After installation, the explosive welding assembly was placed in the explosive tank. The installation structure is shown in Fig. 1.

In order to study the interface forming mechanism of titanium-aluminum composite plate, the composite plate was cut by wire cutting, and the interface morphology was observed under OM (Leica DM4M) and SEM (Hitachi FlexSEM 1000), and the element content of bonding zone was analyzed by EDS (20 kV). Wire cutting machine was used to cut the composite plate test block, which was then ground by sandpaper with different particle size and finally mixed with 10 mL  $H_2O$ , 1 mL  $HNO_3$ , and 3 mL HF to form cauterant.

### 2.2 Interface characteristic simulation

When the adiabatic coefficient  $\gamma$  of explosive is 2.5, the collision between the fly and base is simplified into a one-dimensional throwing model, and then, the collision velocity  $v_p$  of composite plate can be calculated by the following equation [18, 19]:

$$v_p = 1.2v_d \cdot \frac{\left(1 + \frac{32}{27}R\right)^{\frac{1}{2}} - 1}{\left(1 + \frac{32}{27}R\right)^{\frac{1}{2}} + 1} \quad (1)$$

where  $v_d$  is detonation velocity,  $\text{m}\cdot\text{s}^{-1}$ , and  $R$  is the mass ratio of explosive to fly plate.

After the collision velocity of the composite plate is calculated by using Formula (1), the collision angle  $\beta$  is calculated according to the parameter relationship of the horizontally mounted construction [20]:

$$v_p = 2v_c \sin\left(\frac{\beta}{2}\right) \quad (2)$$

where  $v_c$  is the moving speed of the collision point of the composite plate, which can take detonation velocity when the structure is installed in parallel,  $\text{m}\cdot\text{s}^{-1}$ .

**Table 2** Chemical composition of 5083 aluminum plate

Elements	Fe	Ti	Si	Mn	Zn	Mg	Gr	Cu	Al
Content/%	0.4	0.03	0.4	0.4–1.0	0.25	4.0–4.9	0.05	0.1	Bal.

**Fig. 1** Schematic diagram of explosive welding setup



In order to accurately focus on the collision process in explosive welding, the collision velocity  $v_p$  and collision angle  $\beta$  calculated by the above formula are used to establish a collision model of the fly and base plate without explosives [21]. The 2D model was established by ANSYS/AUTODYN, and the smooth-particle hydrodynamics (SPH) method was used to simulate the mechanical problems of continuum such as plate collision [22, 23]. The composite plate was made of TA2 titanium with a thickness of 1.5 mm. The base plate was made of 5083 aluminum with its thickness being 8 mm. The particle size of the model was 0.02 mm × 0.02 mm, and there were 237,500 particles in total. The model structure is shown in Fig. 2.

Mie-Grüneisen equation of state is used for TA2 titanium plate. Mie-Grüneisen equation of state describes the basic relationship between particle velocity and collision velocity, and the formula for calculation is as follows [24]:

$$P = P_H + \Gamma_\rho \rho_0 (e - e_H) \tag{3}$$

$$\Gamma_\rho = \Gamma_0 \rho_0 \tag{4}$$

$$P_H = \frac{\rho_0 c_0^2 \mu (1 + \mu)}{[1 - (s - 1)\mu]^2} \tag{5}$$

$$e_H = \frac{\mu \rho_H}{2\rho_0(1 + \mu)} \tag{6}$$

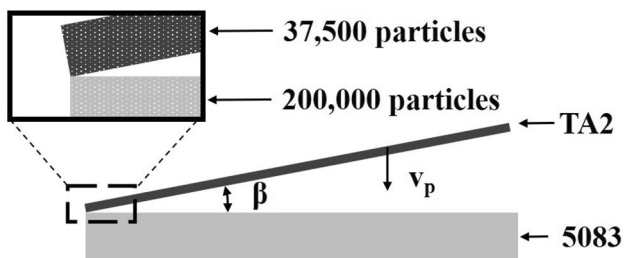


**Fig. 2** Inclined impact configuration of TA2 titanium-5083 aluminum

$$\mu = \frac{\rho - \rho_0}{\rho_0} \tag{7}$$

where  $\rho$  is material density,  $\text{g}\cdot\text{cm}^{-3}$ ;  $\Gamma_0$  is the Grüneisen coefficient;  $\rho_H$  is the current density,  $\text{g}\cdot\text{cm}^{-3}$ ;  $\rho_0$  is the initial density of the material,  $\text{g}\cdot\text{cm}^{-3}$ ;  $c_0$  is volumetric sound velocity,  $\text{km}\cdot\text{s}^{-1}$ ; and  $s$  is the compression ratio. The specific parameters of the Mie-Grüneisen equation of state of TA2 titanium are shown in Table 3.

Steinberg Guinan material model is selected, and the formula of shear modulus  $\mu_\sigma$  and flow stress  $Y$  before material melting is proposed in this model [25].

$$\mu_\sigma = \mu_0 \left[ 1 + bpV^{\frac{1}{3}} - h(T - 300) \right] \tag{8}$$

$$Y = [Y_0(1 + \beta \bar{\epsilon}^p)^n] \left[ 1 + bpV^{\frac{1}{3}} - h(T - 300) \right] \tag{9}$$

where  $\bar{\epsilon}^p$  is equivalent plastic strain,  $V$  is the relative volume,  $Y_0$ ,  $\beta$ ,  $n$ ,  $\mu_0$ ,  $b$ ,  $h$ , and  $T$  is the medium constant. The specific parameters of the Steinberg–Guinan material model of TA2 titanium are shown in Table 4.

The Johnson–Cook material model and linear equation of state are used for 5083 aluminum of the base plate, and the formula for calculation is as follows [26, 27]:

$$\sigma = (A + B\epsilon_p^n) (1 + C \ln \epsilon_p^*) (1 - T^{*m}) \tag{10}$$

$$T^* = (T_0 - T_r) / (T_m - T_r) \tag{11}$$

where  $\epsilon_p$  is the effective plastic strain,  $\epsilon^* P$  is the effective plastic strain rate,  $A$ ,  $B$ ,  $C$ ,  $m$ , and  $n$  are the constants associated with materials,  $T^*$  is the dimensionless temperature,  $T_0$  is particle temperature,  $T_r$  is indoor temperature,  $K$ , and  $T_m$  is melting point,  $K$ . The specific parameters of the Johnson–Cook material model of 5083 aluminum are shown in Table 5.

**Table 3** Mie-Grüneisen equation of state parameter of TA2

Materials	$c/(km\cdot s^{-1})$	$S_1$	$\Gamma_0$	$T_r/K$
TA2	5.020	1.536	1.23	300

**Table 4** Steinberg–Guinan material model parameters for TA2 titanium

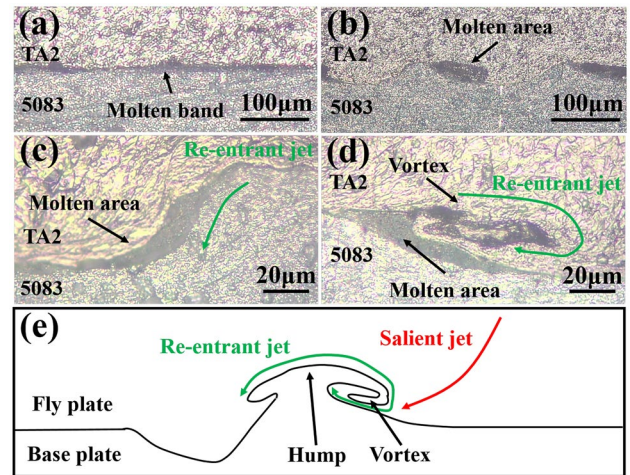
Materials	$\rho/\text{kg}\cdot\text{m}^{-3}$	$A/\text{GPa}$	$B/\text{GPa}$	$n$	$T_m/\text{K}$
TA2	4510	0.85	0.210	0.1	2260

## 3 Results and discussion

### 3.1 Formation of vortices and melted area

The OM image of the titanium–aluminum composite plate interface is shown in Fig. 3. Figure 3a is located at the starting point of the composite plate; the interface of the composite plate is a straight line. The charge thickness of explosive welding was small, so it requires some distance to reach a stable detonation velocity after initiation [28]. The detonation velocity was lower at the initiation end, and correspondingly, the impact energy produced by the collision between titanium plate and aluminum plate was small. Part of the kinetic energy was converted into material heat, melting the interface metal at high temperature. However, the small impact energy was not enough to produce a large range of strong plastic deformation ( $\approx 50\ \mu\text{m}$ ) [29, 30]. The molten metal generated by the collision was more in the form of high-speed jet, and its interior contained both titanium and aluminum materials. In the process of the high-speed movement of the jet, new molten metals were constantly added, and some molten metals were also withdrawn. The rate of withdrawal of molten metal gradually decreases. Over time ( $\approx 10^{-7}\ \text{s}$ ), it cooled at a flat interface, eventually forming the molten band shown in black [16]. Therefore, it can be observed that there is a uniform melting layer at the interface with an average thickness of  $12\ \mu\text{m}$ .

Figure 3b shows the microscopic image of the bonding surface of the composite plate far from the initiation point. Here, the interface changes from straight line to waveform, and the average wavelength is  $200\ \mu\text{m}$ . When the welding explosive reached the stable detonation velocity, the collision velocity reached the lower limit of collision velocity [18]. There was enough impact energy at the interface, the impact pressure of the material was far greater than the yield stress, and the plastic deformation at the interface of the fly and base plate led to the waveform combination of the composite plate. According to Bahrani-Black-Crossland theory [31], salient jet and reentrant jet mainly existed at the interface of waveform combination. The salient jet was mainly generated by high-speed ( $\approx 658\ \text{m}\cdot\text{s}^{-1}$ ) movement of

**Fig. 3** Metallographic image of Ti–Al composite plate. **a** Initiation point, **b** far from the initiation point, **c** wave front, **d** wave back, and **e** vortex formation schematic of the Bahrani-Black-Crossland theory

the composite plate, while the reentrant jet was composed of molten metal at the interface produced by collision [18]. During the movement of reentrant jet, it was affected by the salient jet, and the jet cooled in wave front and wave back to form the molten area. The sufficient contact between titanium and aluminum in the jet created conditions for the formation of molten area, so the molten block in the black area of the wave front can be observed in Fig. 3b.

To further investigate the microstructure evolution of the interface, the local area of the waveform is amplified. Figure 3c shows the wave front of the interface waveform; it can be seen that part of the molten block also exists in the wave back. The reentrant jet at the hump usually had a higher velocity, so the molten metal seldom stayed at the hump and is thin when it cooled. There was a great pressure at the collision point of the composite plate, and the collision of the fly plate compressed the trough of the base plate, so the thickness of the molten area at the trough was relatively thin. The pressure at the hump and trough pushed the metal together, making it stay for a longer while in the wave-waist region, so the wave-waist molten area in Fig. 3c is thicker.

Figure 3d is a metallographic image of the wave-back position of the composite plate, and it shows that some molten metal also exists. Unlike the molten area at the wave-front position, the molten metal at the wave-back interface formed a vortex in which titanium grains are observed. The direction of the reentrant jet deflected under the action of the salient jet, and the molten metal in the jet cooled at the

**Table 5** Johnson–cook material model parameters for 5083 aluminum

Materials	$\rho/\text{kg}\cdot\text{m}^{-3}$	$A/\text{GPa}$	$B/\text{GPa}$	$n$	$C$	$m$	$T_m/\text{K}$
5083	2700	0.167	0.596	0.551	0.001	0.859	893

wave-back position after wrapping part of the titanium [5, 31]. Therefore, titanium side particles are observed inside the vortex in Fig. 3d, which can verify the accuracy of the Bahrani-Black-Crossland theory. Figure 3e shows the vortex formation of the Bahrani-Black-Crossland theory. The deflection effect of the salient jet on the reentrant jet is an important cause of vortex formation [21].

### 3.2 Composition of vortices and molten area

Further studies on the wave-back position of the interface waveforms of Ti–Al composite plate are conducted in Fig. 4. Figure 4a shows the single waveform of the Ti–Al composite plate. It can be seen that some dark molten metal is accumulated at the wave-back position. This was because the high temperature of melting metal increases the diffusion of metal elements [32, 33]. The proportions of the elements inside the molten metal changed, enabling it to present different colors under a light microscope. To better observe the molten area, the orange box in Fig. 4a was zoomed in, as shown in Fig. 4b. Figure 4b shows the contact pattern between the molten region near the hump and the tissue on the titanium side. It should present a horizontal state without stress, but there is angular contact, which is caused by either the downward sloping force or the salient jet. Further study was conducted on the tissue near the vortex. The yellow box in Fig. 4a was amplified, as shown in Fig. 4c. It can be seen that the molten metal is broken in small pieces and enters the titanium tissue after leaving the molten metal body. During the movement of the reentrant jet, the molten metal in

it presented fluid properties [21]. The fluid had weak resistance to its own deformation and breakage, and a small part of the fluid might disengage when it moved at high speed. The detached molten metal dispersed into the titanium tissue, forming the molten area at the periphery of the vortex observed in Fig. 4c. The appearance of small molten blocks scattered in the titanium tissue explains the relative velocity difference between the molten metal and the titanium tissue. Because of the difference in velocity and viscosity, the molten blocks were stripped by the titanium tissue at lower velocity. The blue box in Fig. 4a was zoomed in, as shown in Fig. 4d. It can be observed that the outer layers present a darker color of the molten metal, while the color of the inner tissues is close to that of titanium. Different from the titanium structure of the composite plate, the color inside the vortex is darker, which might be caused by element diffusion and the formation of intermetallic compounds [3]. During vortex formation, the outer layer had higher velocity, and the molten metal in the outer layer contacted more with the titanium tissue. Therefore, element diffusion and intermetallic compounds were more likely to form, leading to darker color of the outside of the vortex than that of the inside. The green box inside the vortex in Fig. 4a was zoomed in, as shown in Fig. 4e. The metallographic structure of some grains can be observed, which might be formed after the cooling of Ti–rich molten metal [12, 16].

### 3.3 Elemental analysis of vortex and melted area

The sample of Ti–Al composite plate after explosive welded was observed under scanning electron microscope, as shown in Fig. 5. Figure 5a shows the microscopic morphology of the wave-back position of the interface waveform. Consistent with the results of metallographic images, the molten area formed by the reentrant jet wave was observed at the interface, which wrapped the titanium to form vortices. The yellow box in Fig. 5a was zoomed in, as shown in Fig. 5b. Points 1–5 were the point scanning positions of EDS, and the line indicated the scanning position. The blue box in Fig. 5a was zoomed in, as shown in Fig. 5c. It can be seen that there are inclined downward ripples in the figure, which might be formed after the salient jet cooling.

Table 6 shows the EDS point scanning results. Points 1 and 4 show the chemical composition of molten metal in the outer layer of the vortex. The content ratio of Ti element, Al element, and Mg element in the outer layer of vortex was approximately 30:10:1. The elements Ti and Al in the molten metal in the outer layer of the vortex were close to 3:1, revealing the formation of  $Ti_3Al$  intermetallic compounds [14, 17].  $Ti_3Al$  has high oxidation resistance at high temperature [34, 35]. According to the formula of critical collision velocity and the formula of critical collision point movement velocity, titanium material has excellent tensile

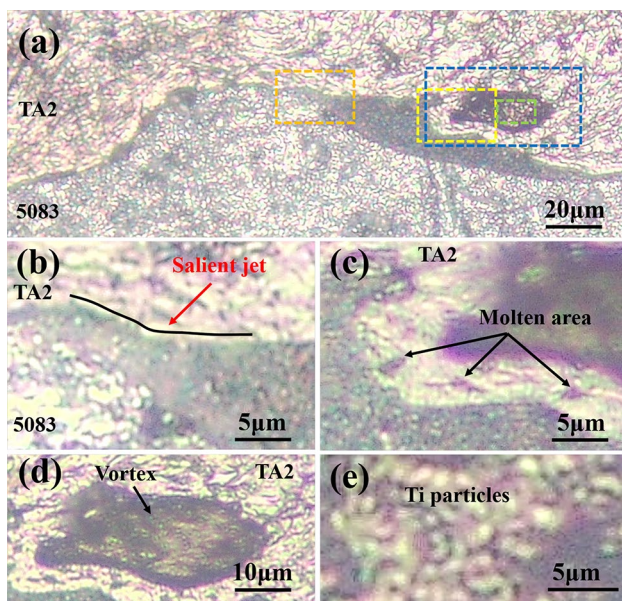


**Fig. 4** High magnification metallographic image of Ti–Al composite plate. **a** Single waveform. **b** Contact pattern. **c** The tissue near the vortex. **d** Vortex. **e** The inside of the vortex

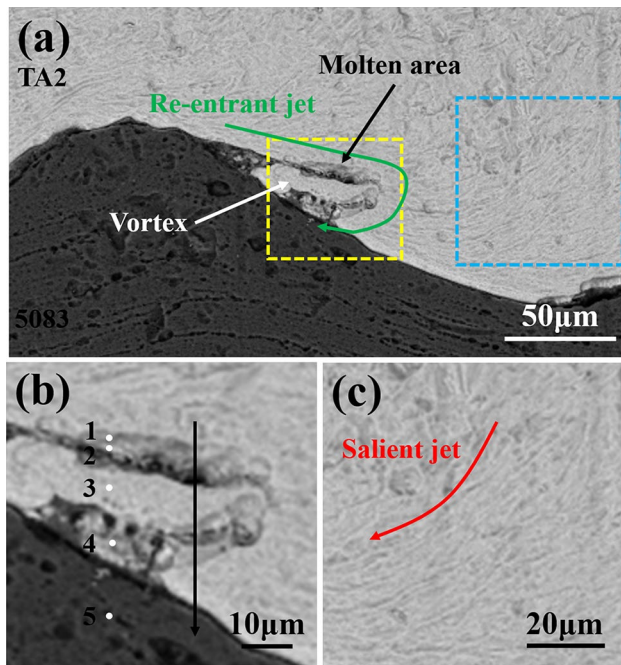


**Fig. 5** SEM images of the Ti–Al composite plate. **a** Wave back. **b** Scanning position of EDS. **c** Salient jet

strength and hardness, which would require greater impact velocity and impact point movement velocity in titanium–aluminum explosive welding [32]. Higher collision velocity and movement velocity of collision point might not enable the gas in the clearance of composite plate to be discharged in time, resulting in air residue on the welding surface. Isolated titanium atoms would absorb part of O element to form  $\text{TiO}_2$  oxides when exposed to air at high temperature, and the high temperature and jet velocity existing in the molten metal would accelerate the formation of oxides [36]. However,  $\text{Ti}_3\text{Al}$  was formed in the outer layer of vortex of the composite plate, and its oxidation resistance would cause the air to be unable to form oxides with titanium. Therefore, it would continue to remain at the bonding surface in the form of gas, which would lead to the formation of cracks. This might be one of the reasons why cracks in the molten area end in titanium tissue observed in other studies [12, 14]. Point 2 also exists in the outer layer of vortex, but the content of Ti element increases significantly. It may be that

**Table 6** Interface chemical composition of Ti–Al composite plate

Element	Ti (atomic fraction %)	Al (atomic fraction %)	Mg (atomic fraction %)
1	67.4	30.0	2.6
2	93.7	5.2	1.0
3	96.7	2.3	1.0
4	72.6	24.9	2.5
5	0.5	92.8	6.6

the reentrant jet washed away the titanium particles from the composite plate. Small particles are constantly melting into the molten metal at high temperature, but the faster cooling of the bonding surface contributed to its presence. Observation of titanium particles confirms the existence of jet. Point 3 shows the chemical composition of the inner layer of the vortex, where the Ti element content reaches the maximum of the molten metal. Inside the vortex is a large titanium tissue wrapped by molten metal, which had little contact with the molten metal. The Al element and Mg element in the inner layer of the vortex mostly came from the element diffusion caused by high temperature. Point 5 is located in the base material close to the bound surface, which is similar to the composition of 5083 aluminum plate in Table 2. It has a very small amount of Ti, which was due to element diffusion from the composite plate.

Al and Mg elements exist in the outer and inner layers of the vortex, which might form intermetallic compounds such as  $\text{Mg}_{17}\text{Al}_{12}$  and  $\text{Mg}_{23}\text{Al}_{30}$  [37]. The formation ratio can be reflected in the element ratio. The ratio of Al element and Mg element in the outer layer of the vortex is close to 10:1, which might generate more  $\text{Mg}_{23}\text{Al}_{30}$ . However, the ratio of two elements inside the vortex is 2:1, which would lead to the increase of  $\text{Mg}_{17}\text{Al}_{12}$  content. The Gibbs free energy of  $\text{Mg}_{23}\text{Al}_{30}$  is smaller than that of  $\text{Mg}_{17}\text{Al}_{12}$  [39]. Therefore,  $\text{Mg}_{23}\text{Al}_{30}$  has good thermal stability and is more likely to exist at high temperature [39]. The proportion of Al and Mg elements in the outer layer of the vortex is higher, which indicates that the temperature in the outer layer of the vortex may be higher than that in the inner region.

EDS line scanning results are shown in Fig. 6. It was found that there is a transition layer between the vortex and Ti structure, which presents a uniform thickness of 5  $\mu\text{m}$ .

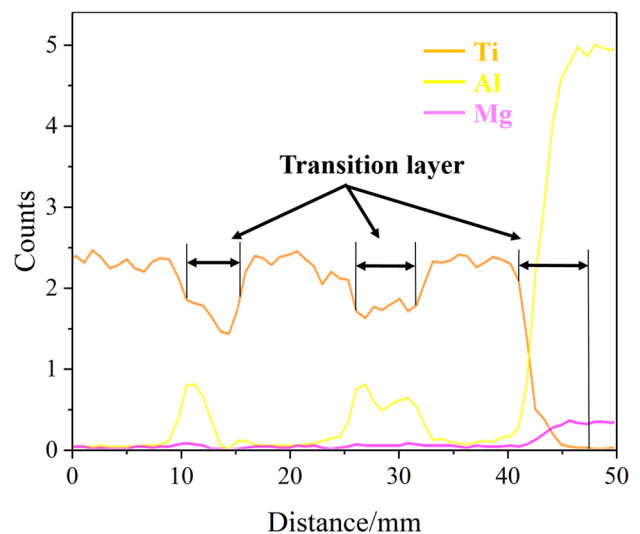


**Fig. 6** Line scanning results of Ti–Al composite plate

However, the thickness of transition layer between the fly and base plate is nearly 8  $\mu\text{m}$ . Compared with the vortex, the collision of the bond surface was more direct, resulting in its higher temperature. Element diffusion was more intense at high temperature, which thickened the transition layer of the bonding surface [15].

### 3.4 Interfacial characterization

According to Formula (1), the collision velocity of the welding model used in the experiment was calculated to be  $658.6 \text{ m}\cdot\text{s}^{-1}$ . According to Formula (2) and combined with the moving velocity of the collision point of  $2478 \text{ m}\cdot\text{s}^{-1}$ , the collision angle of the model was calculated to be  $15.3^\circ$ . The model parameters were set according to the calculated collision velocity and collision angle, and the collision simulation of the fly and base was carried out. The results are shown in Fig. 7. Figure 7a is a simulated image of the interface of Ti–Al composite plate, and it was found that metal jet exists on the interface. The jet can remove the oxide layer and impurities on the welding surface of composite plate and improve the welding effect of composite plate [24]. It is worth noting that the jet particles were mostly 5083 aluminum. This is because the lower the density, the easier it was to form jets. The density of 5083 aluminum at  $2700 \text{ kg}\cdot\text{m}^{-3}$  is much lower than that of TA2 titanium at  $4510 \text{ kg}\cdot\text{m}^{-3}$ , so the jet was mostly composed of aluminum. This is consistent with the research of Wang et al. [24]. Figure 7b shows the particle velocities at the interface. The velocity of the jet reached  $3000 \text{ m}\cdot\text{s}^{-1}$ , which was even higher than the moving velocity of the collision point of the composite plate at  $2478 \text{ m}\cdot\text{s}^{-1}$ . Vortex and molten blocks could occur at this jet velocity, as shown in Fig. 4c. Figure 7c shows the temperature field distribution at the

interface of the composite plate [21]. It was found the interface temperature of the composite plate was extremely high, up to 2100 K, which exceeded the melting point of 1941 K of TA2 titanium and 873 K of 5083 aluminum. After the fly plate collided with the base plate at high speed, the kinetic energy was partially converted into the internal energy of the interface in a very short time, resulting in extremely high temperature of the welding interface. Thus, for some time after the collision, the interface metal flowed in liquid form. Compared with the vortex at the wave-back position, the temperature of the metal jet on the bonding surface was higher. This results in a thicker transition layer on the bonding surface, which is consistent with EDS analysis. Figure 7d shows the interface density image after a certain time of collision. It was found there was a layer of density of  $4.1 \text{ g}\cdot\text{cm}^{-3}$  in the interface. The density of the layer was placed between the two materials, and the thickness was relatively uniform. This may be due to residual stress at the interface, resulting in increased density under compression.

## 4 Conclusions

The explosive welding between TA2 titanium and 5083 aluminum plates was studied by means of experiment and numerical simulation. OM, SEM, and EDS were used to observe the interface microstructure of titanium/steel composite plate. ANSYS/AUTODYN was used to calculate the interface characteristics of microstructure simulated by SPH method, and the following conclusions could be obtained:

1. The pressure at the humps and troughs simultaneously pushed the molten metal, enabling it to stay in the wave-waist region more. There was a relative velocity difference between vortex and titanium tissue, which would lead to fragmentation in the vortex tissue. The outer layer of the vortex had a higher velocity than the inner layer, and the molten metal in the outer layer contacted more with the titanium tissue.
2.  $\text{Ti}_3\text{Al}$  was generated in the vortex of the composite plate, and its oxidation resistance would prevent the air from blending into the titanium layer, which would lead to the formation of cracks. Consider soldering in a vacuum environment or adding an intermediate layer to reduce interfacial defects. The outer layer of the vortex had higher temperature than the inner region. The vortex had a uniform transition layer with a thickness of  $5 \mu\text{m}$ , which was thinner than that of  $10 \mu\text{m}$  between the TA2 titanium and 5083 aluminum.
3. The jet was mostly composed of aluminum, and the interface jet velocity reached  $3000 \text{ m}\cdot\text{s}^{-1}$ . The interface temperature of the composite plate could reach up to 2100 K, which led to the melting of titanium and alu-

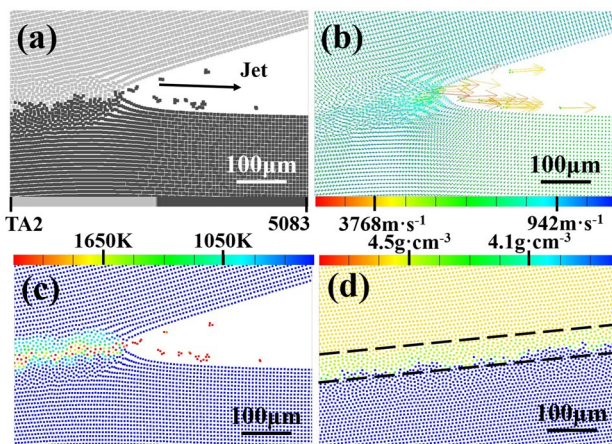


**Fig. 7** Interfacial characterization of Ti–Al composite plate. **a** Simulated image. **b** The interfacial particle velocities. **c** The temperature field distribution. **d** The interface density image

minimum. Compared with the molten metal in the wave-back vortex, the jet temperature at the interface was higher, resulting in a thicker transition layer at the bonding surface. Decreasing the thickness of the explosive within the weldability window can reduce interfacial melting.

**Author contribution** ZB conceived and designed the experiments and wrote the paper; XL performed the experiments and analyzed the experimental data. TZ designed and carried out explosive welding experiments. QW, KR, XD, and YW co-wrote the paper. All authors have read and agreed to the published version of the manuscript.

**Funding** This research was sponsored by National Natural Science Foundation of China (grant number 11872002), Natural Science Foundation of Anhui Province (1808085QA06), and Postdoctoral Foundation of Anhui Province (2019B355).

**Availability of data and materials** Not applicable.

## Declarations

**Ethics approval** Not applicable.

**Consent to participate** Not applicable.

**Consent for publication** Not applicable.

**Conflict of interest** The authors declare no competing interests.

## References

1. Becker N, Gauthier D, Vidal EE (2020) Fatigue properties of steel to aluminum transition joints produced by explosion welding. *Int J Fatigue* 139:105736. <https://doi.org/10.1016/j.ijfatigue.2020.105736>
2. Xu JF, Yang M, Ma HH, Shen ZW, Chen ZJ (2020) Fabrication and performance studies on explosively welded CuCrZr/316L bimetallic plate applied in extreme environments. *J Mater Res Technol* 9:8971–8884. <https://doi.org/10.1016/j.jmrt.2020.05.115>
3. Paul H, Chulist R, Lityńska-Dobrzyńska L, Prazmowski M, Faryna M, Mania I, Szulc Z, Miszczyk MM, Kurek A (2021) Interfacial reactions and microstructure related properties of explosively welded tantalum and steel sheets with copper interlayer. *Mater Des* 208:109873. <https://doi.org/10.1016/j.matdes.2021.109873>
4. Li JX, Panton B, Liang SX, Vivek A, Daehn G (2020) High strength welding of NiTi and stainless steel by impact: process, structure and properties. *Mater Today Commun* 25:101306. <https://doi.org/10.1016/j.mtcomm.2020.101306>
5. Yang M, Ma HH, Shen ZW, Huang ZH, Tian QC, Tian J (2020) Dissimilar material welding of tantalum foil and Q235 steel plate using improved explosive welding technique. *Mater Des* 186:108348. <https://doi.org/10.1016/j.matdes.2019.108348>
6. Sun ZR, Shi CG, Shi H, Li F, Gao L, Wang GZ (2020) Comparative study of energy distribution and interface morphology in parallel and double vertical explosive welding by numerical simulations and experiments. *Mater Des* 195:109027. <https://doi.org/10.1016/j.matdes.2020.109027>
7. Wu XM, Shi CG, Fang ZH, Lin SL, Sun ZR (2021) Comparative study on welding energy and Interface characteristics of titanium-aluminum explosive composites with and without interlayer. *Mater Des* 197:109279. <https://doi.org/10.1016/j.matdes.2020.109279>
8. Sun ZR, Shi CG, Xu F, Feng K, Zhou CH, Wu XM (2020) Detonation process analysis and interface morphology distribution of double vertical explosive welding by SPH 2D/3D numerical simulation and experiment. *Mater Des* 191:108630. <https://doi.org/10.1016/j.matdes.2020.108630>
9. Böhm M, Kowalski M (2020) Fatigue life estimation of explosive cladded transition joints with the use of the spectral method for the case of a random sea state. *Mar Struct* 71:102739. <https://doi.org/10.1016/j.marstruc.2020.102739>
10. Zhao H (2020) Characterization of the microstructure and bonding properties of zirconium-carbon steel clad materials by explosive welding. *Scanning* 2020:1–8. <https://doi.org/10.1155/2020/8881898>
11. Lu LY, Su Y, Chen J, Fang Y, Xia XY, Yu J (2020) Study on microstructure and properties of TA1-304 stainless steel explosive welding cladding plate. *Mater Res Express* 7:026557. <https://doi.org/10.1088/2053-1591/ab7357>
12. Zhang TT, Wang WX, Yan ZF, Zhang J (2021) Interfacial morphology and bonding mechanism of explosive weld joints. *Chin J Mech Eng-En* 34(8):1–12. <https://doi.org/10.1186/s10033-020-00495-7>
13. Chulist R, Fronczek DM, Szulc Z, Wojewoda-Budka J (2017) Texture transformations near the bonding zones of the three-layer Al/Ti/Al explosively welded clads. *Mater Charact* 129:242–246. <https://doi.org/10.1016/j.matchar.2017.05.007>
14. Qin L, Wang J, Wu Q, Guo XZ, Tao J (2017) In-situ observation of crack initiation and propagation in Ti/Al composite laminates during tensile test. *J Alloys Compd* 712:69–75. <https://doi.org/10.1016/j.jallcom.2017.04.063>
15. Cui Y, Liu D, Fan MY, Deng GP, Sun LX, Zhang Y, Chen D, Zhang ZW (2020) Microstructure and mechanical properties of TA1/3A21 composite plate fabricated via explosive welding. *Mater Sci Technol* 36(4):425–433. <https://doi.org/10.1080/02670836.2019.1706905>
16. Fronczek DM, Chulist R, Lityńska-Dobrzyńska L, Lopez GA, Wierzbicka-Miernik A, Schell N, Szulc Z, Wojewoda-Budka J (2017) Microstructural and phase composition differences across the interfaces in al/ti/al explosively welded clads. *Metall Mater Trans A* 48A:4154–4165. <https://doi.org/10.1007/S11661-017-4169-8>
17. Kwasniak P, Garbacz H (2021) Ab initio study of the influence of alloying elements on stability and mechanical properties of selected  $Ti_xAl_y$  intermetallic compounds and their  $Ti_xAl_y/Al$ ,  $Ti_xAl_y/Ti$  interfaces in explosively welded metal–metal composites. *Metall Mater Trans A* 52A:5032–5042. <https://doi.org/10.1007/S11661-021-06449-5>
18. Deribas AA, Kudinov M, Fl M, Simonov VA (1967) Determination of the impact parameters of flat plates in explosive welding. *Combust Explos Shock Waves* 3(2):182–186. <https://doi.org/10.1007/BF00748745>
19. Deribas AA, Kudinov M, Fl M (1967) Effect of the initial parameters on the process of wave formation in explosive welding. *Combust Explos Shock Waves* 3:344–348. <https://doi.org/10.1007/BF00741684>
20. Hoseini-Athar MM, Tolaminejad B (2015) Weldability window and the effect of interface morphology on the properties of Al/Cu/Al laminated composites fabricated by explosive welding. *Mater Des* 86:516–525. <https://doi.org/10.1016/j.matdes.2015.07.114>
21. Yang M, Xu JF, Ma HH, Lei MZ, Ni XJ, Shen ZW, Zhang BY, Tian J (2021) Microstructure development during explosive welding of metal foil: morphologies, mechanical behaviors and mechanisms. *Compos B* 212:108685. <https://doi.org/10.1016/j.compositesb.2021.108685>



22. Chu QL, Zhang M, Li JH, Yan C (2017) Experimental and numerical investigation of microstructure and mechanical behavior of titanium/steel interfaces prepared by explosive welding. *Mater Sci Eng A* 689:323–331. <https://doi.org/10.1016/j.msea.2017.02.075>
23. Wang X, Zheng YY, Liu HX, Shen ZB, Hu Y, Li W, Gao YY, Guo C (2012) Numerical study of the mechanism of explosive/impact welding using smoothed particle hydrodynamics method. *Mater Des* 35:210–219. <https://doi.org/10.1016/j.matdes.2011.09.047>
24. Wang Q, Li XJ, Shi BM, Wu Y (2020) Experimental and numerical studies on preparation of thin AZ31b/AA5052 composite plates using improved explosive welding technique. *Metals* 10:1023. <https://doi.org/10.3390/met10081023>
25. Zhang XP, Luo BQ, Wu G, Wang GJ, Tan FL, Zhao JH, Sun CW (2018) Yield behavior of polystyrene at strain rate  $10^6/s$  under quasi-isentropic compression. *Mech Mater* 124:1–6. <https://doi.org/10.1016/j.mechmat.2018.05.003>
26. Akbari-Mousavi SAA, Riahi M, Hagh-Parast A (2007) Experimental and numerical analyses of explosive free forming. *J Mater Process Technol* 187–188:512–516. <https://doi.org/10.1016/j.jmatprotec.2006.11.208>
27. Rushton N, Schleyer GK, Clayton AM, Thompson S (2008) Internal explosive loading of steel pipes. *Thin Wall Struct* 46:870–877. <https://doi.org/10.1016/j.tws.2008.01.027>
28. Kwiecien I, Wierzbiicka-Miernik A, Szczerba M, Bobrowski P, Szulc Z, Wojewoda-Budka J (2021) On the disintegration of A1050/Ni201 explosively welded clads induced by long-term annealing. *Materials* 14:2931. <https://doi.org/10.3390/ma14112931>
29. Zhou Q, Liu R, Zhou Q, Chen PW, Zhu L (2021) Microstructure characterization and tensile shear failure mechanism of the bonding interface of explosively welded titanium-steel composite. *Mater Sci Eng A* 820:141559. <https://doi.org/10.1016/j.msea.2021.141559>
30. Zeng XY, Li XQ, Li XJ, Mo F, Yan HH (2019) Numerical study on the effect of thermal conduction on explosive welding interface. *Int J Adv Manuf Tech* 104:2607–2617. <https://doi.org/10.1007/s00170-019-04054-w>
31. Bahrani AS, Black TJ, Crossland B (1967) The mechanics of wave formation in explosive welding. *Proc R Soc Lond A* 296:1445. <https://doi.org/10.1098/rspa.1967.0010>
32. Wu XM, Shi CG, Feng K, Gao L, Li WX, Qian K (2021) Experimental and numerical approach to titanium-aluminum explosive welding. *Mater Res Express* 8:096503. <https://doi.org/10.1088/2053-1591/ac2017>
33. Ye CQ, Zhai WG, Lu GY, Liu QS, Ni L, Ye L, Fang X (2021) Effect of secondary explosive welding on microstructure and mechanical properties of 10CrNi<sub>3</sub>MoV steel-based composite plates. *Metall Mater Trans A* 52A:1568–1573. <https://doi.org/10.1007/s11661-021-06190-z>
34. Knaislova A, Novak P, Cabibbo M, Jaworska L, Vojtech D (2021) Development of TiAl-Si alloys—a review. *Materials* 14(4):1030. <https://doi.org/10.3390/ma14041030>
35. Yin YC, Zhu S, Chang Q, Wang WY, Gao GY, Wang XM, Yang S, Han GF (2021) Improved wear resistance and mechanical properties of Al matrix with TiAl-based coatings. *Surf Eng* 37(11):1440–1448. <https://doi.org/10.1080/02670844.2021.1971431>
36. Lawson S, Baamran K, Newport K, Alghamadi T, Jacobs G, Rezaei F, Rowanaghi AA (2022) Integrated direct air capture and oxidative dehydrogenation of propane with CO<sub>2</sub> at isothermal conditions. *Appl Catal B* 303:120907. <https://doi.org/10.1016/j.apcatb.2021.120907>
37. Froncze DM, Chulist R, Litynska-Dobrzynska L, Kac S, Schell N, Kania Z, Szulc Z, Wojewoda-Budka J (2017) Microstructure and kinetics of intermetallic phase growth of three-layered A1050/AZ31/A1050 clads prepared by explosive welding combined with subsequent annealing. *Mater Des* 130:120–130. <https://doi.org/10.1016/j.matdes.2017.05.051>
38. Sun L, Hui W, Zhou Y, Zhai WY, Dong H, Liu YM, Gao Q, Dang MH, Peng JH (2020) The electronic structural and elastic properties of Mg<sub>23</sub>Al<sub>30</sub> intermediate phase under high pressure. *Curr Comput-Aided Drug Des* 10(8):642. <https://doi.org/10.3390/cryst10080642>
39. Zheng B, Zhao L, Hu XB, Dong SJ, Li H (2019) First-principles studies of Mg<sub>17</sub>Al<sub>12</sub>, Mg<sub>2</sub>Al<sub>3</sub>, Mg<sub>2</sub>Sn, MgZn<sub>2</sub>, Mg<sub>2</sub>Ni and Al<sub>3</sub>Ni phases. *Phys B* 560:255–260. <https://doi.org/10.1016/j.physb.2018.11.067>

**Publisher's note** Springer Nature remains neutral with regard to jurisdictional claims in published maps and institutional affiliations.

Springer Nature or its licensor holds exclusive rights to this article under a publishing agreement with the author(s) or other rightsholder(s); author self-archiving of the accepted manuscript version of this article is solely governed by the terms of such publishing agreement and applicable law.